Erschienen in: Nature. Springer. 2025, 642(8069), S. 947-953
https://doi.org/10.1038/s41586-025-09092-x

Article

A soft-clamped topological waveguide for phonons

Xiang Xi[1,2]✉, Ilia Chernobrovkin[1,2], Jan Košata[3,5], Mads B. Kristensen[1,2], Eric Langman[1,2], Anders S. Sørensen[1,2], Oded Zilberberg[4] & Albert Schliesser[1,2]✉

Topological insulators were originally discovered for electron waves in condensed-matter systems. Recently, this concept has been transferred to bosonic systems such as photons[1] and phonons[2], which propagate in materials patterned with artificial lattices that emulate spin-Hall physics. This work has been motivated, in part, by the prospect of topologically protected transport along edge channels in on-chip circuits[2,3]. In principle, topology protects propagation against backscattering, but not against loss, which has remained limited to the dB cm^{-1} level for phononic waveguides, whether topological[4–7] or not[8–19]. Here we combine advanced dissipation engineering[20]—in particular, the recently introduced method of soft clamping[21]—with the concept of valley-Hall topological insulators for phonons[22–26]. This enables on-chip phononic waveguides with propagation losses due to dissipation of 3 dB km^{-1} at room temperature, orders of magnitude below any previous chip-scale devices. The low losses also allow us to accurately quantify backscattering protection in topological phononic waveguides, using high-resolution ultrasound spectroscopy. We infer that phonons follow a sharp, 120° bend with a 99.99% probability instead of being scattered back, and less than one phonon in a million is lost. Our work will inspire new research directions on ultralow-loss phononic waveguides and will provide a clean bosonic system for investigating topological protection and non-Hermitian topological physics.

Phonons are the excitations of sound in a solid or liquid. Compared with photons or electrons, they feature slow propagation speed, strong confinement in materials and immunity to electromagnetic radiation. These properties are fuelling the prospect of chip-scale phononic circuits, which route, store and process classical or quantum information in more compact, efficient and robust ways[27,28]. Over the past decade, a growing community of researchers has thus investigated and refined the properties of the elementary building block of this circuitry: a low-loss waveguide for phonons. Work towards this goal has covered a wide range of frequencies, ranging from the ultrasonic[5,8–10,13] (about 20 kHz–100 MHz) to the hypersonic[11,12,14–19,29,30] (about 100 MHz–10 GHz) domain. However, propagation losses have remained relatively high (≥dB $cm^{-1} = 10^5$ dB km^{-1}; Fig. 1), limiting the range of applications.

Recently, these efforts have been enriched markedly by the uptake of ideas from topological physics. Non-trivial topological properties of sound propagation in materials patterned with suitable artificial crystal structures have been investigated[2], mirroring similar effects for light studied in topological photonics[1]. Here, analogies with quantum spin- and valley-Hall physics are of fundamental interest—in particular, the existence of edge modes that guide excitations at the interface between two non-equivalent topological insulators[31–33]. A more practical motivation lies in the promise of reduced backscattering within these edge modes in the presence of certain perturbations, such as sharp bends—a highly desirable feature for a waveguide, especially in complex circuits. Recent implementations have provided some empirical evidence for this protected transport[4,6,7,23–25], yet quantitative measurements of backscattering are scarce[26]. Furthermore, topological protection does not entail low losses. Existing topological phononic waveguides are lossy (Fig. 1b), which has remained an open challenge[2].

We address the above challenges for phononic waveguides by drawing on the recently achieved marked advances in diluting the dissipation of nanomechanical resonators using high stress[20]. In particular, we harness the method of soft clamping[21], here characterized by a smooth exponential mode confinement. It suppresses both radiation loss to the substrate and internal dissipation due to material bending and has triggered an avalanche of work that culminated in mechanical resonators with quality factors (Q) above 10^{10} (refs. 20,34). The ultralow loss of these localized, non-propagating phononic modes has enabled many applications in quantum opto-mechanics[35–37] and electro-mechanics[38].

In this work, we show how the concepts of topological phonon transport and soft clamping naturally coalesce: transverse to their propagation direction, the topological edge modes penetrate evanescently into the bulk crystal, giving rise to the soft confinement that is at the heart of soft clamping[21]. In a suitably patterned

[1]Niels Bohr Institute, University of Copenhagen, Copenhagen, Denmark. [2]Center for Hybrid Quantum Networks, Niels Bohr Institute, University of Copenhagen, Copenhagen, Denmark. [3]Institute for Theoretical Physics, ETH Zürich, Zurich, Switzerland. [4]Department of Physics, University of Konstanz, Konstanz, Germany. [5]Present address: Hitachi Energy Research, Baden-Dättwil, Switzerland. ✉e-mail: xiang.xi@nbi.ku.dk; albert.schliesser@nbi.ku.dk

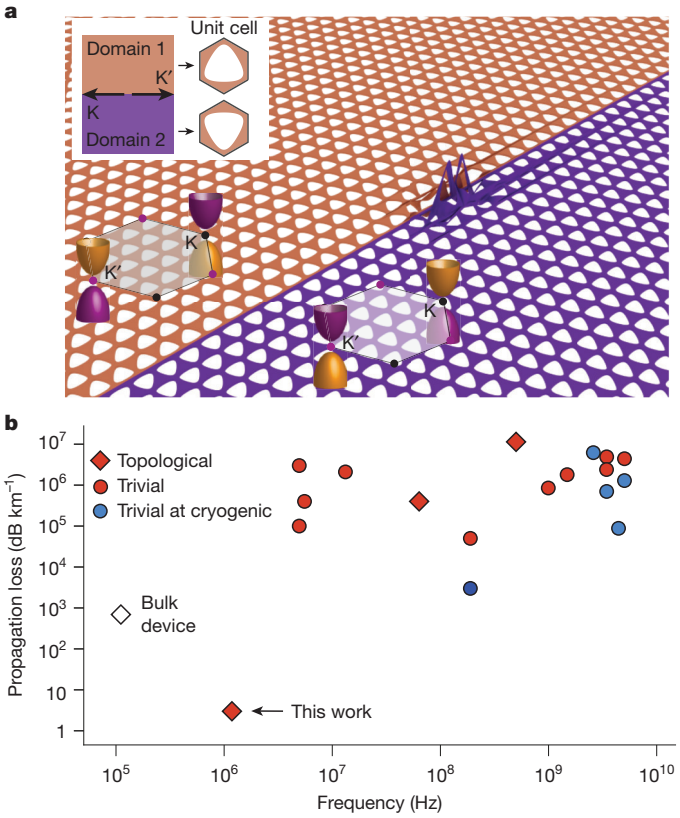

Fig. 1 | A topological waveguide for phonons with ultralow loss. a, Rendering of an out-of-plane vibration mode guided along the interface of two topologically distinct domains, realized by patterning a thin, stressed membrane with a regular array of holes. The top inset shows the two different phononic crystal unit cells of the two domains. The bottom insets show dispersion curves in the Brillouin zone near the K and K′ points. The band inversion between the two different domains is characteristic of a valley-Hall topological waveguide. **b**, Propagation loss of acoustic waves as reported in the literature. Red indicates experiments at room temperature, light blue at cryogenic temperatures above 4 K and deep blue at the millikelvin level. Diamonds[5–7] represent topological devices, whereas circles[8–19] represent non-topological systems. Filled markers indicate on-chip devices and open markers indicate bulk devices.

high-stress membrane, we thus obtain ultrasonic waveguides with propagation loss due to dissipation down to 3 dB km^{-1}, many orders of magnitude lower than anything demonstrated at ultra- or hypersonic frequency to date (Fig. 1). Remarkably, the loss is comparable to superconducting waveguides for microwaves[39] and approaches that of optical fibres. The low loss also allows us to accurately quantify the very small amount of backscattering in a waveguide that includes sharp (120°) bends, by high-resolution ultrasound spectroscopy of a waveguide wrapped up into a triangular cavity. We conclude that the bends dominate backscattering, with an average probability of only 1.1×10^{-4}. That is, about 99.99% of the phonon energy flows around an individual bend.

A pre-stressed phononic valley-Hall insulator

In this work, we implement topological phononic waveguides in 20-nm-thin silicon nitride (SiN) membranes under high tensile stress (about 1.2 GPa), as required for dissipation dilution[40]. The phonon modes of interest are flexural vibrations out of the membrane plane (Fig. 1a). We adapt the valley-Hall effect that has been used successfully to demonstrate topological modes in linear media[22–26] to a stressed membrane by patterning the membrane with a periodic array of holes. The holes are arranged on a honeycomb lattice whose basis vectors $\mathbf{a}_1$ and $\mathbf{a}_2$ are $a = 200$ µm long (Fig. 2a). Each hole is a rounded triangle with a circumradius $r \approx 93$ µm. The symmetry axis of the triangle and a honeycomb lattice vector subtend an angle θ (Fig. 2a).

This geometry implies a rotational symmetry C_3. For $\theta = 0°$, an additional mirror symmetry yields the point group C_{3v} (ref. 41). In phonon momentum space, doubly degenerate Dirac cones then form at the **K** and **K′** points on the edge of the first Brillouin zone, similar to graphene-like structures[42]. For $\theta \neq n \times 2\pi/6$ ($n \in \mathbb{N}$), the mirror symmetry around the axes defined by the lattice vectors $\mathbf{a}_1$ and $\mathbf{a}_2$ is broken[42]. This lifts the double degeneracy to create a bandgap (Fig. 2b,d). In the vicinity of the **K** point, the local band structure can be modelled with a perturbative Dirac Hamiltonian $H = v_D(\delta k_x \tau_2 + \delta k_y \tau_1) + m\tau_3$, where v_D is an effective group velocity, δk_x and δk_y are the quasimomenta relative to **K**, m is an effective mass term and the τ_i are the Pauli matrices. The corresponding eigenvalues $E_\pm = \pm[v_D^2(\delta k_x^2 + \delta k_y^2) + m^2]^{1/2}$ form hyperboloid sheets centred at the **K** point, separated by $2m$, which therefore quantifies the bandgap. Time-reversal symmetry implies that a similar band structure forms at the **K′** point (Fig. 1a, inset). In the following, we are predominantly concerned with the propagation of phonons whose wave vector is located in one of these so-called valleys, that is, close to the **K** or **K′** points.

At the **K** point, the associated eigenfunctions $\psi^+_{p_1}$ and $\psi^-_{p_2}$ feature vortices with opposite chirality centred at two inequivalent triangular-lattice sites p_1 and p_2 in real space (Fig. 2b–e). Crucially to our work, inverting the triangle orientation $\theta \to -\theta$ leaves the band structure intact but inverts the symmetry-breaking perturbation, that is, transforms $+m \to -m$. This mass inversion enforces a band inversion, switching the vorticity of the valley states (Fig. 2b–e). The two bulk crystals with opposite m are topologically distinct: they cannot be continuously deformed into one another without closing the gap.

To obtain a localized topological edge mode, we construct at a zigzag interface between two bulks with $\theta = +30°$ and $\theta = -30°$, respectively (Fig. 2f). The changing sign of the mass term m across the interface entails a topological chiral edge mode within the gap at each valley, according to the bulk-boundary correspondence (Supplementary Information), which is confirmed in numerical simulation (Fig. 2g). Modes propagating along the edge are hence located close to either the **K** or **K′** valleys (with quasilinear dispersion), depending on their propagation direction. Backscattering is expected to be suppressed due to the large required transfer of quasimomentum, available only in structures that break the crystal symmetry[2,43]. The edge mode is localized to the interface (Fig. 2h). Transverse to the propagation direction, it decays exponentially with a decay length $L_c \approx 280$ µm (Fig. 2h), thus providing soft mode confinement. Taking into account the non-trivial relaxation of the pre-stress in the device design, we fabricated the devices and measured the phononic band diagram (Fig. 2i and Methods). The measured results agree well with the simulated results. This confirms the existence of phononic valley edge states in our SiN membranes in the presence of high stress.

Ultralow-loss phonon propagation

The successful implementation of topological edge states in highly stressed thin membranes sets an expectation of low propagation loss, following dissipation dilution theory[40]. Physically, this is enabled by storing a large fraction about $D_n/(D_n + 1)$ of the total mode energy in a loss-less potential W_n^{tens}, namely, the elongation of the material against the static tensile stress, induced by the geometric nonlinearity of the material. Only the energy stored in membrane bending W_n^{bend} is lossy; a fraction around $2\pi/Q_{\mathrm{int}}$ of it is dissipated each cycle. Here, $Q_{\mathrm{int}} = E_1/E_2$ is the material-dependent intrinsic quality factor (the ratio of the real (E_1) and imaginary (E_2) parts of the elastic modulus). Together, this leads to a dilution of losses by the factor $D_n \approx W_n^{\mathrm{tens}}/W_n^{\mathrm{bend}} \gg 1$, with a resulting mode Q-factor of $Q_n = D_n Q_{\mathrm{int}}$. Large dilution factors can be

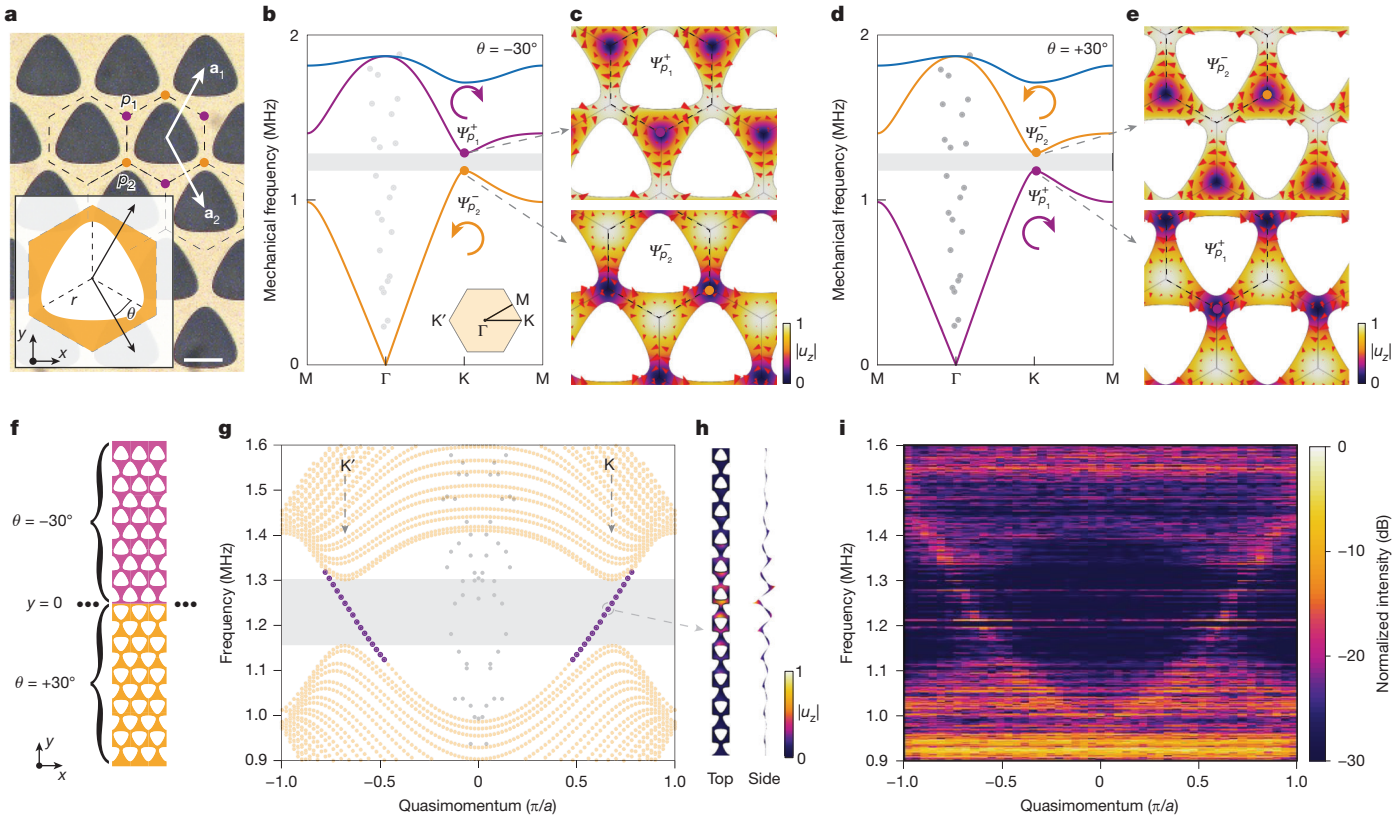

Fig. 2 | Valley-Hall topological insulators and edge states in a thin stressed membrane. a, Microscope image of fabricated phononic valley-Hall crystals in an SiN membrane. Hexagonal unit cells of the honeycomb lattice are superimposed with the two inequivalent sites p_1 and p_2, as well as the basis vectors $\mathbf{a}_1$ and $\mathbf{a}_2$. The inset shows a single unit cell with a rounded triangular hole of circumradius r and orientation θ in the centre. **b**,**d**, Simulated energy band diagrams for the crystals with $\theta = -30°$ (**b**) and $\theta = +30°$ (**d**). At the K point, the valley states $\psi^{\pm}_{p_1,p_2}$ have a clockwise (+) or anticlockwise (−) energy flow, with vortices centred at sites p_1 and p_2. **c**,**e**, Simulated modal profiles of the states $\psi^{+}_{p_1}$ and $\psi^{-}_{p_2}$ in **b** and **d**. The colour code represents $|u_z|$, the out-of-plane mechanical displacement field, and the red arrows represent the energy flow. **f**, Design of the domain interface that accommodates topological edge states. **g**, Simulated band diagram of the topological structure in **f**. The yellow, purple and grey dots represent bulk modes, topological edge modes and in-plane mechanical modes, respectively. Additional boundary modes localized at the rims of the membrane are not presented. **h**, Top and side views of simulated spatial distributions of the topological edge states at the K point. **i**, Measured band diagram of the topological insulator along the topological domain interface. Scale bar, 100 μm (**a**).

reached in strongly stressed, thin membranes, whose mode geometry minimizes bending[40] (Supplementary Information).

Engineering mode geometry to minimize bending is the basic idea of soft clamping[21]. Confining vibrational modes to defects in phononic crystals has proven extraordinarily effective in this regard, as the mode can penetrate evanescently into the crystal. It thereby softly transitions to low amplitudes away from the defect. This avoids the sharp kink—and therefore very large bending—usually present at the clamp, where the membrane is suspended from its frame[40]. Given the exponential decay of the topological edge modes into the bulk, soft clamping would be expected in our devices. Together with the high stress, and small thickness, large dilution factors are expected. Although exponential decay of edge modes has also been present in previous works, they involve hard clamping in each unit cell[4,6,23,24], are unstressed[7,26], or both. Here, we avoid these issues by fully suspending a thin stressed membrane with a topological waveguide pattern.

We thus anticipate that edge mode phonons propagate over distances much longer than any feasible chip size and assess the loss in a topological waveguide wrapped up into a closed triangular path (Fig. 3a). Each side of the triangle is 15 unit cells long in the first batch of samples and 19 unit cells long in the second batch of samples. At the three corners, sharp 120° bends connect the sides. Importantly, the geometry of the bends largely conserves the crystal symmetry. The distance of the triangular cavity to the membrane rim exceeds 2,000 μm $\gg L_c$, which prompts us to neglect radiation loss in the following.

The closed triangular path selects a set of discrete resonant modes with longitudinal wave numbers $k_n^{\parallel} = 2\pi n/L$, where n is an integer and $L \approx 9.3$ mm is the round-trip length of the samples with a side length of 15 unit cells. Through the waveguide dispersion (compare Fig. 2g), the discrete set of allowed wavenumbers maps to a set of well-defined frequencies $\{\Omega_n\}$, at which an edge mode oscillates. These modes of wave numbers $k_n^{\parallel}$ are measured from the **Γ** point, and the wave numbers with frequency near the centre of the bandgap correspond to the **K** point. Without external actuation, we measure a thermal spectrum (Fig. 3b) of the out-of-plane displacement at a location along the topological edge (Methods). It shows a series of sharp peaks close to the frequencies $\{\Omega_n\}$ inside an otherwise quiet region, corresponding to the bandgap. Peaks around any one Ω_n appear in pairs, the origin of which will be discussed below. More dense and irregular peaks are seen outside the bandgap. These correspond to bulk modes. We also measured the spatial localization of these topological modes (Methods), with an example shown in Fig. 3c, which confirms that the topological edge modes are well-confined near the topological interface.

The propagation loss α for waves guided along the edge sets a lower limit for the rate Γ_n, at which the energy of the phonons circulating in the triangular cavity is dissipated. On this basis, we can relate measurements of the mode quality factors of the triangular cavity, $Q_n = \Omega_n/\Gamma_n$, to the propagation loss in the waveguide due to mechanical dissipation by $\alpha_n \lesssim \Omega_n/Q_n v_g$ (refs. 11,12). Here, we use the simulated mid-gap value $v_g = 280$ m s^{-1} for the group velocity. We determine the Q_n of the

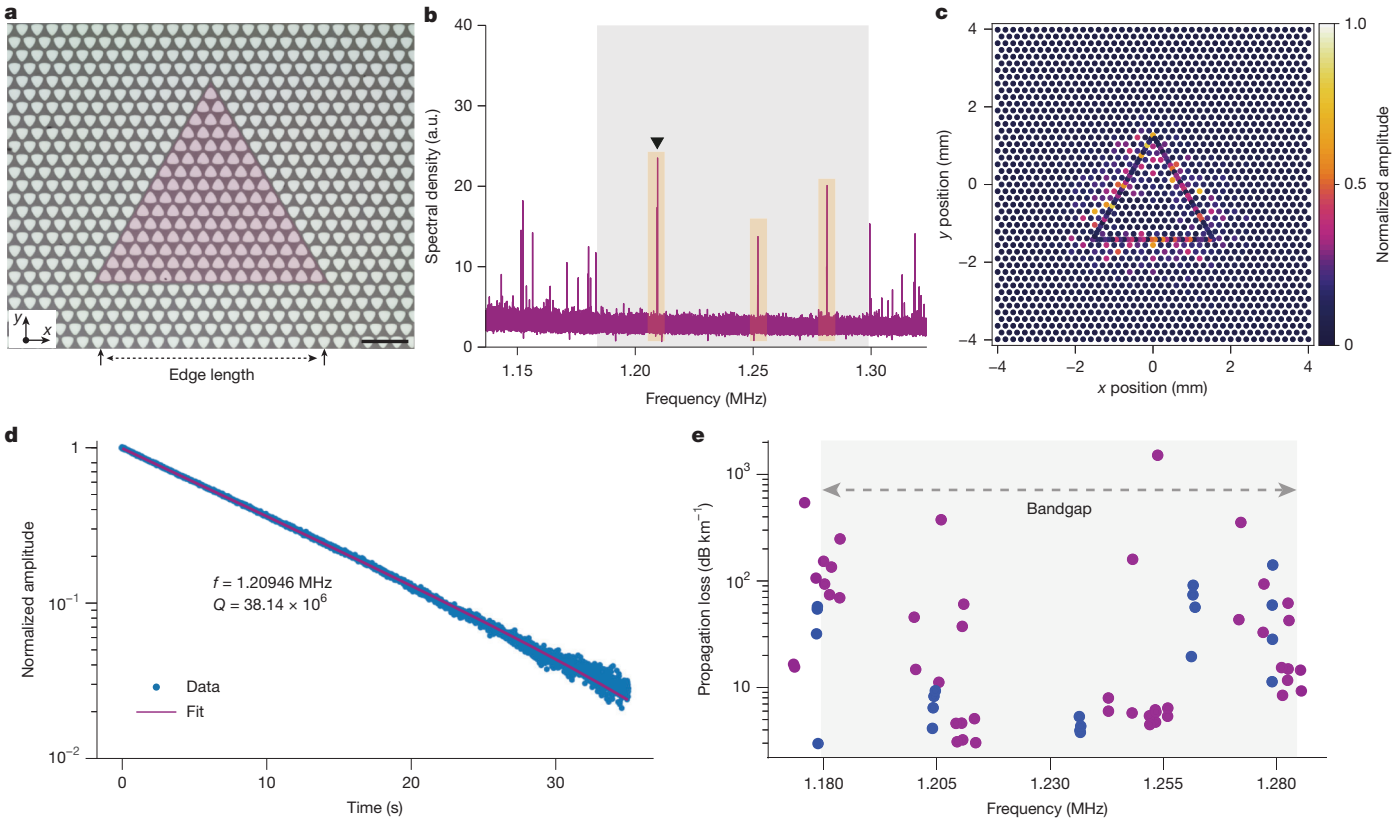

Fig. 3 | Triangular-waveguide phononic cavities with ultralow loss. **a**, Microscope image of a topological phononic waveguide wrapped up into a triangular cavity. Side length is 15 unit cells. **b**, Thermomechanical noise spectrum measured on a waveguide cavity as shown in **a**. The grey shaded area indicates the bulk bandgap. **c**, Spatial map of thermomechanical noise amplitude at a cavity resonance frequency (marked with a triangle in **b**), confirming localization to the domain interface. **d**, Ringdown measurement of one of the cavity modes (marked with a triangle in **b**). **e**, Propagation loss of edge modes due to dissipation inferred from measurements on several triangular cavities with edge length of 15 (purple) or 19 (blue) unit cells. The shaded region indicates an averaged bandgap, whose frequency may vary by 15 kHz from device to device. Scale bar, 600 μm (**a**). a.u., arbitrary units.

modes with ringdown measurements (Methods), with an example shown in Fig. 3d. We observe a high quality factor of $Q_n = 38.1 \times 10^6$ for a cavity mode at $\Omega_n \approx 2\pi \times 1.21$ MHz, corresponding to a propagation loss of less than 3.1 dB km^{-1}. This is a remarkably low loss, even more so for an on-chip waveguide. Measuring the loss in many devices (Fig. 3e), we find some statistical scatter, similar to that of soft-clamped zero-dimensional resonators[21]. In the following analysis, we focus on samples in which at least one mode has a Q-factor above 10^7, as we consider lower quality factors throughout all modes as an indicator of fabrication failure with broken membrane tethers or excessive contamination. Other typical fabrication imperfections, such as sidewall roughness, are not expected to markedly affect the quality factor. The modes near the edge or outside of the bandgap present systematically higher loss, probably because of hybridization with modes at the membrane rim.

Through finite element simulation, we evaluate the dilution factors D_n in the range of 10,000–25,000 for the different in-gap modes. Together with the intrinsic quality factor[44] $Q_{\mathrm{int}} \approx 1{,}140$ for the 20-nm thick SiN membranes used in this work, we obtain quality factors well compatible with our measurements (Fig. 3 and Supplementary Information). Simulations also confirm that hard-clamped waveguides in similarly stressed membranes[13] with similar wavenumber are limited to much higher propagation loss (Supplementary Information).

It is instructive to recast the quality factor of the triangular phonon cavity as a finesse using $\mathcal{F}_n = Q_n \times \Omega_{\mathrm{FSR}}/\Omega_n$, with the free spectral range $\Omega_{\mathrm{FSR}}/2\pi = v_g/L$. For the mode with the highest Q-factor, we obtain a cavity finesse of $\mathcal{F}_n \approx 1.3 \times 10^6$, on par with the highest finesse that can be realized for an optical cavity using dielectric mirrors[45]. With the round-trip loss given by $\pi/\mathcal{F}$, we can further infer that when passing a sharp bend—of which there are three per round trip—less than about 0.8 ppm of phonons are lost on average. This is a stark illustration of the fact that phonons cannot be scattered to free-space modes, a common limitation in optical cavities[46], and that scattering to other modes in the device is strongly suppressed, not least by the absence of other modes in the gap.

Quantifying backscattering

Closer inspection of the measured and simulated spectra shows that the in-gap modes occur in pairs (Fig. 4a), whose frequencies $\Omega_n^{\pm}$ are separated by a small splitting $\Delta\Omega_n \equiv (\Omega_n^+ - \Omega_n^-) \approx \mathcal{O}(2\pi \times 100\ \mathrm{Hz})$. Owing to time-reversal symmetry, clockwise and anticlockwise propagating edge modes are expected to be degenerate (see also Fig. 2g). However, residual coupling between counterpropagating modes due to backscattering will hybridize the travelling waves into standing waves, with their degeneracy lifted by the coupling[26,43].

The theoretical description of valley-Hall topological systems predicates that the counterpropagating waveguide modes are localized in the inequivalent **K** and **K′** valleys. The required large quasimomentum transfer is, therefore, expected to suppress elastic backscattering—even at sharp bends as long as they preserve crystal symmetry sufficiently well[2,43]. Meanwhile, numerous experiments in both the optical and acoustic domains have qualitatively established guidance in topological edge modes around sharp bends. However, experiments that accurately quantify residual backscattering are very rare—and when conducted, have sometimes yielded seemingly unexpected results[46].

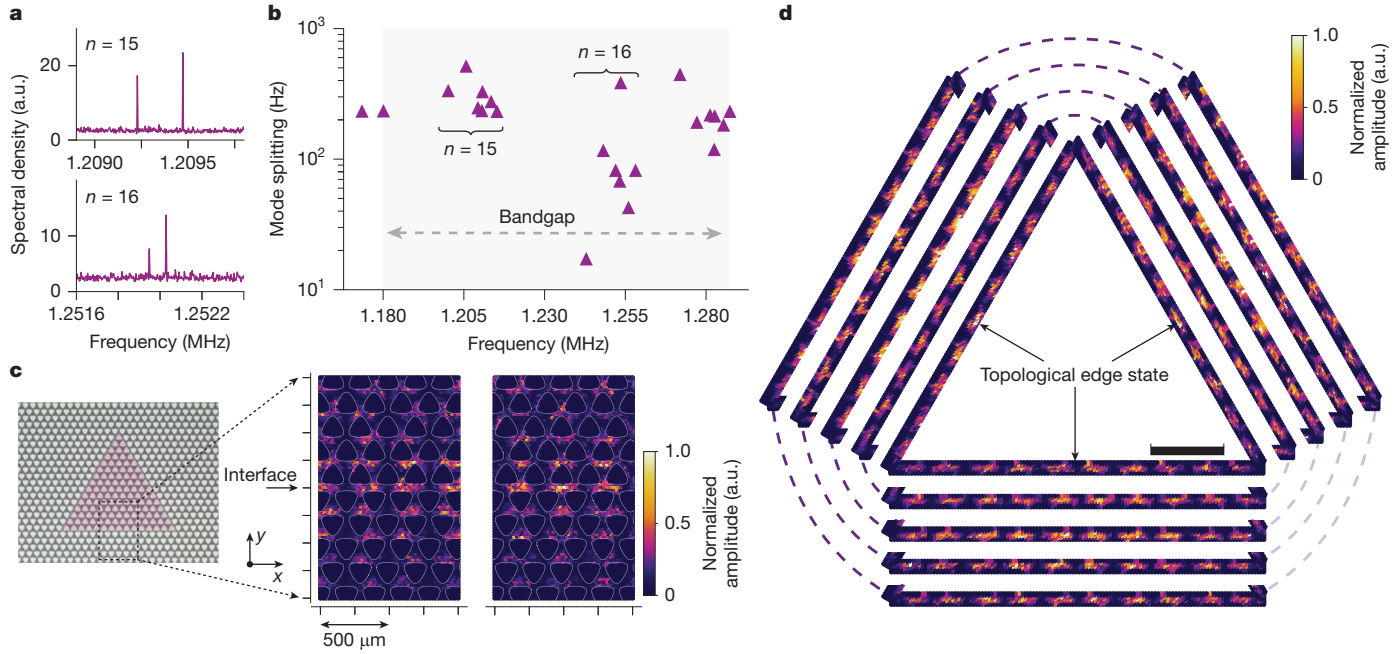

Fig. 4 | Backscattering-induced mode splitting. a, Magnification into the spectral density of Fig. 3b shows small splittings of the cavity modes. **b**, Overview of measured mode splittings from different triangular cavities with an edge length of 15 unit cells. Devices are discarded if all edge modes have $Q_n < 10^7$ (see Supplementary Information for all data). **c**, Spatial map of thermomechanical noise amplitude for the mode pair shown in the top panel of **a**. The positions of nodes and antinodes indicate that the two modes are spatially orthogonal to each other. **d**, Spatial maps of thermomechanical noise amplitude of one of the $n = 15$ edge modes along the waveguide path of the cavity. The maps from five different devices align, suggesting a consistent location of scatterers, namely, the corners. Scale bar, 600 μm (**d**). a.u., arbitrary units.

To our knowledge, the most precise characterization for topological phonon waveguides was obtained recently by a qualitative comparison of simulated and measured cavity spectra, from which a reflection probability $P_{bs} < 5\%$ on passage of a sharp corner was inferred[26].

In our devices, the low loss and associated narrow linewidths $\Omega_n^{\pm}/Q_n^{\pm} \ll 2\pi \times 1$ Hz afford precise spectroscopic resolution of the splittings across a large number of cavity resonances and devices, as shown in Fig. 4b. The splitting is proportional to the round-trip backscattering amplitude, and correspondingly its probability to occur on passage of a single (effective) scatterer in a cavity round-trip can be given as $P_{bs} = (\pi \times \Delta\Omega_n/\Omega_{FSR})^2$ (Supplementary Information). For the smallest measured splitting $\Delta\Omega_n = 2\pi \times 17.2$ Hz, this evaluates to a backscattering probability of $P_{bs}^{min} \approx 2 \times 10^{-6}$ in the whole device.

To refine the understanding of the origin of backscattering, we measure the edge mode pattern under thermal excitation with fine spatial resolution (Methods). Their respective number of antinodes ($2n$) allows assignment of mode numbers to frequencies as $\{\Omega_{n=15}, \Omega_{n=16}, \Omega_{n=17}\} \approx 2\pi\{1.210, 1.255, 1.280\}$ MHz. Magnifying further into a straight waveguide region (Fig. 4c) for patterns of the $\Omega_{n=15}^{\pm}$ mode pair shows that the two standing wave patterns are orthogonal to each other, with antinodes of one mode lining up with the nodes of the other modes. This would be expected for symmetric and anti-symmetric combinations of counterpropagating Bloch waves. Furthermore, we find that the locations of nodes and antinodes are consistent among a series of five samples (Fig. 4d). This supports the notion of scatterers that are reproduced in our fabrication process, and hence probably part of the mask geometry, rather than random disorders introduced by fabrication imperfections or contamination, which could lead to Anderson localization[46]. We also observe that the $\Omega_{n=15}^{\pm}$ modes have either nodes or antinodes pinned to the corners of the triangular phonon cavity. Together, we take this evidence to suggest that backscattering occurs mainly at the three corners of the triangle.

Under this assumption, it can be shown that, owing to interference, the backscattered waves from the corners add up for modes with $(n \bmod 3) = 0$; otherwise, backscattering cancels out for identical scattering amplitudes from each corner (Supplementary Information). This cancellation can well explain the overall lower splitting observed for the $n = 16$ mode pair. However, in real devices, backscattering can occur at randomly distributed perturbations, leading to a larger variation of backscattering. We extract the mean splitting $\Delta\Omega_{n=15}/3$ caused by the passage of one corner. Averaging over all intact (with at least one mode with $Q > 10^7$) samples, we obtain $\langle\Delta\Omega_{n=15}\rangle/3 \approx 2\pi \times 102$ Hz, corresponding to a backscattering probability $P_{bs}^{(\angle)} = 1.1 \times 10^{-4}$ on passage of an individual corner. We suspect the backscattering comes from the slightly broken symmetry due to the different stress distribution at the corner. As a benchmark, we have also simulated the backscattering in a triangular cavity made from a hard-clamped membrane waveguide (Supplementary Information), indicating a backscattering probability of order unity at a corner. This underlines the strong backscattering suppression achieved in our topological phonon waveguides. It should be noted that, although backscattering is low, it is the primary constraint on the propagation length of phonons, rather than low dissipation. For example, the lowest measured splitting of 17.2 Hz would correspond to a backscattering-limited propagation length of 15 m.

Parametric amplification

To date, most of the topological waveguiding systems remain working in the linear regime. However, the nanomechanical devices introduced here also give access to richer physics that occurs in nonlinear and time-modulated potentials. These can give rise to squeezing interaction[47] and parametric amplification[48]. The low loss of our topological phononic waveguides also offers opportunities for exploring the nonlinear phenomena with topological physics. As an experimental example, we subject one of the triangle cavities to a parametric drive force through a piezoelectric actuator at twice the frequency of one of the topological edge modes, which introduces squeezing interaction

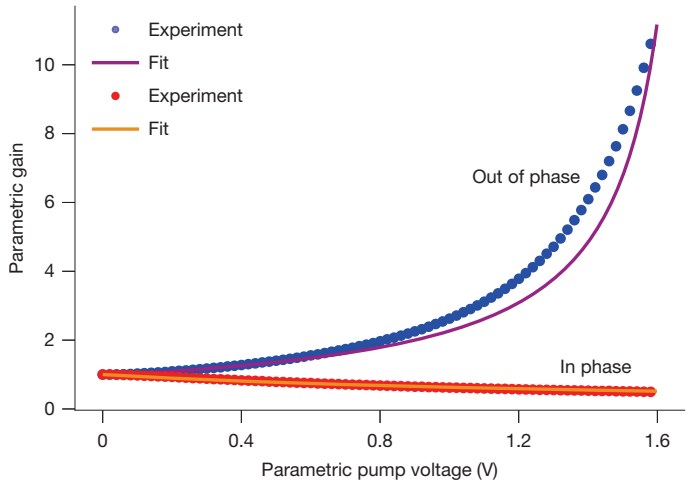

Fig. 5 | Parametric amplification and damping. Measured parametric gain G for in-phase $\psi = 0°$ (red dots and orange line) and out-of-phase $\psi = 90°$ (blue dots and purple line) parametric drive.

and observe phase-dependent amplification of that mode. Figure 5 shows the measured gain $G \equiv |x_{on}|/|x_{off}|$, that is, the ratio of mechanical amplitudes with ($|x_{on}|$) and without ($|x_{off}|$) parametric modulation, respectively (Methods). This feature could form the basis of a topological travelling wave amplifier[49].

Conclusions and outlook

In conclusion, we have realized a chip-based platform that unites topological phonon waveguiding and dissipation dilution. The resulting devices achieve unprecedentedly low propagation loss and very low backscattering even at sharp bends. Our analysis suggests that there is room for further optimization of the dilution factor (Supplementary Information). We, therefore, expect that quality factors and propagation losses can be improved markedly, similar to the exponential gains seen recently in the Q-factors of soft-clamped localized resonators[20]. Backscattering, in turn, may be reduced further by engineering the interface between the bulk crystals[43]. The intrinsic nonlinearity and the possibility to locally change the mechanical potential electrostatically[50] add a host of opportunities for non-Hermitian topological physics, which we have only begun to explore. Single electrodes could implement phase shifters or tunable parametric mode-couplers. Electrode arrays with phase-synchronized drives could provide an architecture for low-noise travelling wave amplification[49], phononic solitons and so on.

1. Ozawa, T. et al. Topological photonics. *Rev. Mod. Phys.* **91**, 015006 (2019).
2. Shah, T., Brendel, C., Peano, V. & Marquardt, F. *Colloquium*: topologically protected transport in engineered mechanical systems. *Rev. Mod. Phys.* **96**, 021002 (2024).
3. Hafezi, M., Demler, E. A., Lukin, M. D. & Taylor, J. M. Robust optical delay lines with topological protection. *Nat. Phys.* **7**, 907–912 (2011).
4. Cha, J., Kim, K. W. & Daraio, C. Experimental realization of on-chip topological nanoelectromechanical metamaterials. *Nature* **564**, 229–233 (2018).
5. Yu, S.-Y. et al. Critical couplings in topological-insulator waveguide-resonator systems observed in elastic waves. *Natl Sci. Rev.* **8**, nwaa262 (2020).
6. Xi, X., Ma, J., Wan, S., Dong, C.-H. & Sun, X. Observation of chiral edge states in gapped nanomechanical graphene. *Sci. Adv.* **7**, eabe1398 (2021).
7. Hatanaka, D. et al. Valley pseudospin polarized evanescent coupling between microwave ring resonator and waveguide in phononic topological insulators. *Nano Lett.* **24**, 5570–5577 (2024).
8. Hatanaka, D., Mahboob, I., Onomitsu, K. & Yamaguchi, H. Phonon waveguides for electromechanical circuits. *Nat. Nanotechnol.* **9**, 520–524 (2014).
9. Hatanaka, D., Dodel, A., Mahboob, I., Onomitsu, K. & Yamaguchi, H. Phonon propagation dynamics in band-engineered one-dimensional phononic crystal waveguides. *New J. Phys.* **17**, 113032 (2015).
10. Cha, J. & Daraio, C. Electrical tuning of elastic wave propagation in nanomechanical lattices at MHz frequencies. *Nat. Nanotechnol.* **13**, 1016–1020 (2018).
11. Fu, W. et al. Phononic integrated circuitry and spin-orbit interaction of phonons. *Nat. Commun.* **10**, 2743 (2019).
12. Patel, R. N. et al. Single-mode phononic wire. *Phys. Rev. Lett.* **121**, 040501 (2018).
13. Romero, E. et al. Propagation and imaging of mechanical waves in a highly stressed single-mode acoustic waveguide. *Phys. Rev. Appl.* **11**, 064035 (2019).
14. Mayor, F. M. et al. Gigahertz phononic integrated circuits on thin-film lithium niobate on sapphire. *Phys. Rev. Appl.* **15**, 014039 (2021).
15. Xu, X.-B. et al. High-frequency traveling-wave phononic cavity with sub-micron wavelength. *Appl. Phys. Lett.* **120**, 163503 (2022).
16. Feng, Z., Liu, Y., Xi, X., Wang, L. & Sun, X. Gigahertz phononic integrated circuits based on overlay slot waveguides. *Phys. Rev. Appl.* **19**, 064076 (2023).
17. Chen, I.-T. et al. Optomechanical ring resonator for efficient microwave-optical frequency conversion. *Nat. Commun.* **14**, 7594 (2023).
18. Zhang, L., Cui, C., Chen, P.-K. & Fan, L. Integrated-waveguide-based acousto-optic modulation with complete optical conversion. *Optica* **11**, 184–189 (2024).
19. Bicer, M. & Balram, K. C. Low-loss GHz frequency phononic integrated circuits in gallium nitride for compact radio frequency acoustic wave devices. *IEEE Trans. Ultrason. Ferroelectr. Freq. Control* **71**, 172–181 (2024).
20. Engelsen, N. J., Beccari, A. & Kippenberg, T. J. Ultrahigh-quality-factor micro- and nanomechanical resonators using dissipation dilution. *Nat. Nanotechnol.* **19**, 725–737 (2024).
21. Tsaturyan, Y., Barg, A., Polzik, E. S. & Schliesser, A. Ultracoherent nanomechanical resonators via soft clamping and dissipation dilution. *Nat. Nanotechnol.* **12**, 776–783 (2017).
22. Lu, J. et al. Observation of topological valley transport of sound in sonic crystals. *Nat. Phys.* **13**, 369–374 (2017).
23. Yan, M. et al. On-chip valley topological materials for elastic wave manipulation. *Nat. Mater.* **17**, 993–998 (2018).
24. Ma, J., Xi, X. & Sun, X. Experimental demonstration of dual-band nano-electromechanical valley-hall topological metamaterials. *Adv. Mater.* **33**, 2006521 (2021).
25. Zhang, Q. et al. Gigahertz topological valley Hall effect in nanoelectromechanical phononic crystals. *Nat. Electron.* **5**, 157–163 (2022).
26. Ren, H. et al. Topological phonon transport in an optomechanical system. *Nat. Commun.* **13**, 3476 (2022).
27. Eggleton, B. J., Poulton, C. G., Rakich, P. T., Steel, M. J. & Bahl, G. Brillouin integrated photonics. *Nat. Photon.* **13**, 664–677 (2019).
28. Safavi-Naeini, A. H., van Thourhout, D., Baets, R. & Laer, R.van Controlling phonons and photons at the wavelength scale: integrated photonics meets integrated phononics. *Optica* **6**, 213–232 (2019).
29. Fang, K., Matheny, M. H., Luan, X. & Painter, O. Optical transduction and routing of microwave phonons in cavity-optomechanical circuits. *Nat. Photon.* **10**, 489–496 (2016).
30. Zivari, A., Stockill, R., Fiaschi, N. & Gröblacher, S. Non-classical mechanical states guided in a phononic waveguide. *Nat. Phys.* **18**, 789–793 (2022).
31. Wu, L.-H. & Hu, X. Scheme for achieving a topological photonic crystal by using dielectric material. *Phys. Rev. Lett.* **114**, 223901 (2015).
32. Khanikaev, A. B. & Shvets, G. Two-dimensional topological photonics. *Nat. Photon.* **11**, 763–773 (2017).
33. Barik, S. et al. A topological quantum optics interface. *Science* **359**, 666–668 (2018).
34. Cupertino, A. et al. Centimeter-scale nanomechanical resonators with low dissipation. *Nat. Commun.* **15**, 4255 (2024).
35. Rossi, M., Mason, D., Chen, J., Tsaturyan, Y. & Schliesser, A. Measurement-based quantum control of mechanical motion. *Nature* **563**, 53–58 (2018).
36. Mason, D., Chen, J., Rossi, M., Tsaturyan, Y. & Schliesser, A. Continuous force and displacement measurement below the standard quantum limit. *Nat. Phys.* **15**, 745–749 (2019).
37. Huang, G., Beccari, A., Engelsen, N. J. & Kippenberg, T. J. Room-temperature quantum optomechanics using an ultralow noise cavity. *Nature* **626**, 512–516 (2024).
38. Seis, Y. et al. Ground state cooling of an ultracoherent electromechanical system. *Nat. Commun.* **13**, 1507 (2022).
39. Kurpiers, P., Walter, T., Magnard, P., Salathe, Y. & Wallraff, A. Characterizing the attenuation of coaxial and rectangular microwave-frequency waveguides at cryogenic temperatures. *EPJ Quantum Technol.* **4**, 8 (2017).
40. Schmid, S., Villanueva, L. G. & Roukes, M. L. *Fundamentals of Nanomechanical Resonators* 2nd edn (Springer, 2023).
41. Košata, J. & Zilberberg, O. Second-order topological modes in two-dimensional continuous media. *Phys. Rev. Res.* **3**, L032029 (2021).
42. Lu, J. et al. Dirac cones in two-dimensional artificial crystals for classical waves. *Phys. Rev. B* **89**, 134302 (2014).
43. Shah, T., Marquardt, F. & Peano, V. Tunneling in the Brillouin zone: theory of backscattering in valley Hall edge channels. *Phys. Rev. B* **104**, 235431 (2021).
44. Villanueva, L. G. & Schmid, S. Evidence of surface loss as ubiquitous limiting damping mechanism in sin micro- and nanomechanical resonators. *Phys. Rev. Lett.* **113**, 227201 (2014).
45. Rempe, G., Thomson, R. J., Kimble, H. J. & Lalezari, R. Measurement of ultralow losses in an optical interferometer. *Opt. Lett.* **17**, 363–365 (1992).

46. Rosiek, C. A. et al. Observation of strong backscattering in valley-Hall photonic topological interface modes. *Nat. Photon.* **17**, 386–392 (2023).
47. Rugar, D. & Grütter, P. Mechanical parametric amplification and thermomechanical noise squeezing. *Phys. Rev. Lett.* **67**, 699–702 (1991).
48. Xi, X., Ma, J. & Sun, X. A topological parametric phonon oscillator. *Adv. Mater.* **37**, 2309015 (2025).
49. Peano, V., Houde, M., Marquardt, F. & Clerk, A. A. Topological quantum fluctuations and traveling wave amplifiers. *Phys. Rev. X* **6**, 041026 (2016).
50. Hälg, D. et al. Strong parametric coupling between two ultracoherent membrane modes. *Phys. Rev. Lett.* **128**, 094301 (2022).

Methods

Fabrication

The membranes were fabricated from stoichiometric SiN film deposited on double-side polished silicon wafers by low-pressure chemical vapour deposition, with a resulting tensile stress of approximately 1.2 GPa. First, we performed spin-coating of a 1.5 μm layer of resist AZ Mir 701 on both sides of the wafer. Second, the resist on one side of the wafer was patterned with phononic crystals and the resist on the other side was patterned with the backside etch windows, by using a Heidelberg MLA150 maskless lithography system. After the development of photoresist using tetramethylammonium hydroxide, each side of the wafer was then subjected to dry-etching with inductively coupled plasma with CF_4/H_2 chemistry, transferring the pattern on the resist to the SiN layer. This entire process is calibrated by focus-exposure array tests to reach an agreement between the mask pattern and the etched pattern to within 50 nm. The membrane pattern is etched into the topside of the wafer, and rectangles are etched into the backside silicon to define the hole to be etched through the silicon to release the membrane on the topside. The extent of each backside rectangle is 707 μm larger than the released geometry on the front side, to account for the etch angle of the KOH. Next, the membranes were released by etching the silicon with KOH wet chemistry. A backside protective holder manufactured by Advanced Micromachining Tools was used to protect the phononic crystal side. Finally, the membranes were cleaned using an H_2SO_4/H_2O_2 mixture for 10 min, followed by a rinse in deionized water and allowed to dry in air.

Measurement

Setup. Extended Data Fig. 1 shows the experimental setup for characterizing the devices. The devices were placed inside a vacuum chamber with a pressure below 10^{-6} mbar at room temperature. A custom-built fibre-based Mach–Zehnder optical interferometer with the probe laser mounted on a programmable motorized stage was used to detect the mechanical motion of the devices across different spatial points[51]. In the interferometer, the output of a 1,550-nm fibre laser was split into a reference beam and a detection beam. The detection beam was focused on the membrane, and its reflection carrying the mechanical motion signal was collected and then mixed with the reference beam through a beam splitter. The waist diameter of the focused beam on the membrane was around 50 μm. The outputs of the beam splitter were recorded by two photodetectors. One of them was connected to the proportional–integral–derivative controller, the output of which was connected to a phase shifter to stabilize the relevant phase between the reference beam and detection beam at the maximized detection efficiency point. Another one was connected to a lock-in amplifier and was used for mechanical signal analysis in both the time and frequency domains.

Measurement of band diagram. The spectral dispersion diagram in Fig. 2i was obtained by measuring the mechanical frequency response to a micro-pin drive while moving the detection laser spot along the topological interface. The micro-pin was gently brought into contact with the membrane near the topological interface, and it was also clamped to a piezoelectric actuator, which was driven by the lock-in amplifier. The presence of the pin strongly increases the mechanical loss, and it was therefore lifted off the surface for the other measurements. Owing to the large loss from the contact pin, the discrete resonance modes were invisible in the measurement. The spatial sampling rate of the laser spot was 8 points per unit cell length. The band diagram was obtained by making a spatial Fourier transform of the frequency response along the topological domain interface. This frequency response is a steady-state measurement from elastic waves travelling back and forth, and naturally carries the phase and amplitude for waves of both directions. Therefore, we can get positive and negative quasimomentum states in the band diagram.

Measurement of spatial modal profiles. The spatial modal profiles were obtained by measuring the thermal spectra of the device across spatial points. In the measurement of the whole device (Fig. 3c), we took one sampling point per lattice site in the bulk crystal region, whereas we took three sampling points per unit cell length along the topological interface line. We took a regular rectangular spatial grid along the selected region with a sampling grid of 20 μm × 20 μm in Fig. 4c and Supplementary Fig. 7, and a rectangular grid along the edge with a mesh of 25 μm × 15 μm in Fig. 4d and Supplementary Fig. 8.

Measurement of the ringdown. For ringdown measurement of the mechanical modes, we used a piezo-electric transducer to shake the sample as a whole, at a frequency that we carefully tuned to match one of the mechanical resonances Ω_n. Once we observed large-amplitude oscillations of one of the modes through the laser interferometer, the excitation was stopped. The amplitude then decayed as proportional to $\exp(-\Gamma_n t/2)$ with time t, which allows us to extract Γ_n from a fit and therefore Q_n.

Measurement of parametric amplification. Parametric amplification or squeezing of a resonant mechanical mode of frequency Ω_n can be realized by adding an external force with frequency of $2\Omega_n$ to the system[52]. In our experiments, this was realized by adding a parametric pump voltage $V_{2\Omega_n}\cos(2\Omega_n t)$ to the piezoelectric actuator that exerts force on the membranes (Extended Data Fig. 1). A small mechanical signal to be amplified was realized by adding a small voltage $V_{\text{signal}}\cos(\Omega_n t+\psi)$ to the piezoelectric actuator. Here Ω_n was chosen to be the frequency of one of the topological edge modes. The displacement gain of this small signal provided by the parametric pump is

$$G=\frac{|x_{\text{on}}|}{|x_{\text{off}}|}=\left[\frac{\cos^2\psi}{(1+V_{2\Omega_n}/V_{\text{th}})^2}+\frac{\sin^2\psi}{(1-V_{2\Omega_n}/V_{\text{th}})^2}\right]^{\frac{1}{2}}, \quad (1)$$

where $|x_{\text{on}}|$ and $|x_{\text{off}}|$ are absolute values of mechanical displacement with and without parametric force, respectively, and V_{th} is the threshold voltage for reaching the region of instability for parametric oscillation. In this preliminary demonstration, we choose a topological edge mode with Q around 1.8×10^7.

Data availability

The data that support the findings of this study in the main text and the Supplementary Information are available at Zenodo[53] (https://doi.org/10.5281/zenodo.15183532).

Code availability

The codes that support the findings of this study are available at Zenodo[53] (https://doi.org/10.5281/zenodo.15183532).

51. Barg, A. et al. Measuring and imaging nanomechanical motion with laser light. *Appl. Phys. B* **123**, 8 (2017).
52. Mashaal, A. et al. Strong thermomechanical noise squeezing stabilized by feedback. *Phys. Rev. Res.* **7**, L012071 (2025).
53. Xi, X. et al. Data and code for "A soft-clamped topological waveguide for phonons". *Zenodo* https://doi.org/10.5281/zenodo.15183532 (2025).

Acknowledgements We acknowledge T. Capelle for the help with micro-fabrication. This work was supported by the European Research Council project PHOQS (grant no. 101002179), the Novo Nordisk Foundation (grant nos. NNF20OC0061866 and NNF22OC0077964), the Danish National Research Foundation (Centre of Excellence 'Hy-Q'), the Independent Research Fund Denmark (grant no. 1026-00345B), the Swiss National Science Foundation (CRSII5 177198/1, CRSII5 206008/1 and PP00P2 163818), the Deutsche Forschungsgemeinschaft (project nos. 449653034 and SFB1432), the Horizon 2020 research and innovation programme of the European Union (the Marie Skłodowska–Curie grant agreement no. 101107341) and a research grant (VIL59143) from the Villum Foundation.

Author contributions X.X. designed the devices and built the setup with contributions from I.C.; X.X. and I.C. conducted the measurements and analysed the data. J.K. and O.Z. contributed to the design at an early stage and developed the topological theory. X.X., J.K.,

M.B.K. and E.L. conducted the numerical simulations. X.X., M.B.K. and A.S. analysed dissipation dilution and soft clamping. E.L. fabricated the devices. A.S.S. contributed to the discussion and understanding of the experimental data. X.X., J.K. and A.S. wrote the paper with input from all the authors. X.X. and A.S. supervised the project.

Competing interests E.L. and A.S. have co-founded the company Qfactory ApS, which commercializes soft-clamped phononic resonators. The other authors declare no competing interests.

Additional information

Correspondence and requests for materials should be addressed to Xiang Xi or Albert Schliesser.

Peer review information *Nature* thanks Jiuyang Lu and the other, anonymous, reviewer(s) for their contribution to the peer review of this work. Peer reviewer reports are available.

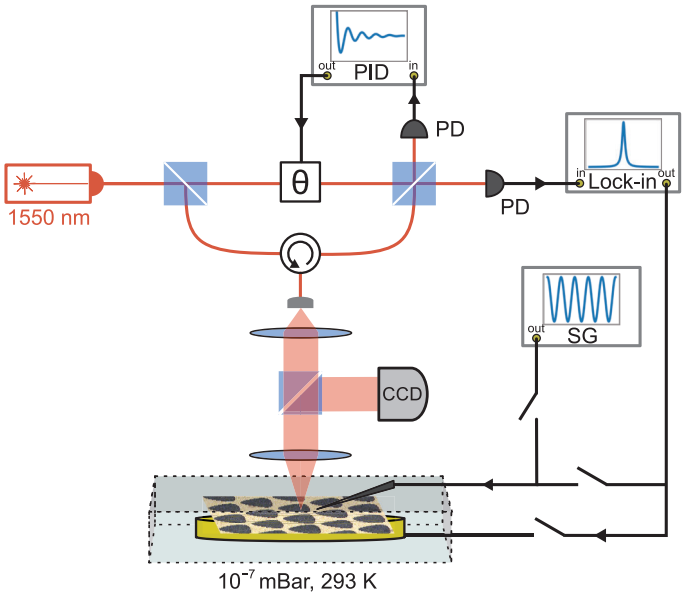

Extended Data Fig. 1 | Experimental setup. Shown is the fiber laser (1550 nm), the two photodetectors (PD), the proportional-integral-derivative (PID) controller (FPGA: Red Pitaya), a phase shifter (θ, piezo fiber stretcher), the lock-in amplifier (lock-in), and a signal generator (SG). The membrane is simultaneously imaged with a CCD camera.